

The Capturing of Ionized Oxygen in Sodium Vanadium Oxide Nanorods Cathodes under Operando Conditions

Mengyu Yan, Luzi Zhao, Kangning Zhao, Qiulong Wei, Qinyou An,* Guobin Zhang, Xiujuan Wei, Wenhao Ren, and Liqiang Mai*

The control of voltage window has been considered as a universal strategy in improving the cycling stability of cathode materials, which is supposed and explained by avoiding side reactions. To address the conjecture, the detailed structure evolution of $\text{Na}_{0.76}\text{V}_6\text{O}_{15}$ nanorods is investigated with different electrochemical reaction voltage windows. High time resolution in situ X-ray diffraction, ex situ X-ray photoelectron spectroscopy, ex situ Raman spectroscopy, and transmission electron microscopy demonstrate the amorphization of $\text{Na}_{0.76}\text{V}_6\text{O}_{15}$ nanorods and formation of ionized oxygen in nanorods, leading to the increased polarization voltage and fast capacity fading. The amorphization and diffusion of ionized oxygen in nanorods is controlled by optimizing the voltage window, resulting in the great increase of capacity retention from 26% to 80%. It is demonstrated that controlling the voltage window and corresponding ionized oxygen diffusion can mitigate the fast capacity fading to achieve long lasting lithium ion batteries.

performance.^[12,21–23] Considerable efforts have been devoted to improving their rate performance and long-term cycling stability. Recent studies show that the electrode performance of pure vanadium oxides can be greatly improved by addition of Na^+ or other second metal cations into these host vanadium oxides.^[12,24–26] These ions can act as “pillars” to increase the framework stability upon lithium insertion/extraction.^[19,27,28] Furthermore, these pillars increase not only the inter-layer space of the materials but also the ion diffusion rate.^[29,30] Yang group has proven that the sodium vanadium oxides can deliver a capacity of 175 mAh g^{-1} after 69 cycles.^[28] Cao group prepared the $\text{Na}_{1.25}\text{V}_3\text{O}_8$ nanobelts retaining 94% of the initial capacity even after 450 cycles at the current density of 200 mA g^{-1} .^[21] All

1. Introduction

Lithium-ion batteries (LIBs) have shown great power in revolutionizing communications and transportation, enabling the rise of smartphones and electric cars with a practical range, which have further extended to large scale energy storage systems and shaken up the electricity grid.^[1–4] However, the limited capacity and high cost of the current commercial cathodes block their further commercial applications.^[5,6] It is of great challenge and importance to explore cathode materials with competitive specific capacity and low cost.^[7]

Over the past decades, vanadium oxides, such as V_2O_5 ,^[8–12] V_2O_4 ,^[13] V_2O_3 ,^[14] VO_2 ,^[15,16] V_6O_{13} ^[17] have attracted much attention as electrode materials for LIBs due to their abundant resources and low cost, as well as high capacities.^[18–20] However, these generally studied bulk vanadium oxides suffer from intrinsic low lithium ion diffusion coefficient, poor electronic conductivity, and inferior long-term cycling

of these literatures demonstrate the sodium vanadium oxide is a promising cathode materials for secondary lithium batteries. Another effective strategy, reducing the electrochemical reaction voltage window, is also widely used to improve the performance of vanadium oxides and other electrode materials.^[31,32] It is considered that the deep lithium ion intercalation/deintercalation may cause the disorder of layered structure, which leads to the fast capacity fading.^[33,34] By reducing the voltage window, the cycling stability of electrode material is improved with the sacrifice of capacity.^[35,36] The aforementioned behavior is traditionally explained with avoiding the side reaction and irreversible reaction.^[37–39] The detailed observation and corresponding understanding under operando condition is still insufficient. The capture of structure evolution of electrode materials under different electrochemical reaction voltage windows is profitable to understand and further optimize the electrochemical performance of vanadium oxides as well as sodium vanadium oxides.

In this work, a new compound among sodium vanadium oxides, $\text{Na}_{0.76}\text{V}_6\text{O}_{15}$ is used to investigate the relationship between electrochemical performance and reaction voltage window by using in situ X-ray diffraction (XRD), ex situ X-ray photoelectron spectroscopy (XPS), ex situ Raman spectroscopy and transmission electron microscopy (TEM). It is demonstrated that the deep intercalation/deintercalation of Li^+ results in the more serious voltage drop, electrochemical polarization, and degenerated electrochemical activity. Moreover, the detailed structure evolution during electrochemical processes is further explored. The $\text{Na}_{0.76}\text{V}_6\text{O}_{15}$ undergoes a two phase reaction

M. Y. Yan, L. Z. Zhao, K. N. Zhao, Dr. Q. L. Wei,
Prof. Q. Y. An, G. B. Zhang, X. J. Wei, W. H. Ren,
Prof. L. Q. Mai
State Key Laboratory of Advanced Technology for
Materials Synthesis and Processing
Wuhan University of Technology
Hubei, Wuhan 430070, China
E-mail: anqinyou86@whut.edu.cn; mlq518@whut.edu.cn



DOI: 10.1002/adfm.201602134

during intercalation process, while a nonequilibrium solid solution reaction during deintercalation processes, under the voltage window of 1.5–4.0 V. The asymmetric electrochemical reaction pathway results in the decrease of ionized oxygen migration energy, which is one of the archcriminal of cyclability. The further electrochemical investigation shows that the $\text{Na}_{0.76}\text{V}_6\text{O}_{15}$ nanorods can deliver a high capacity of 213.5 mAh g^{-1} under the voltage window of 1.5–4.0 V. By optimizing the voltage window to 2.0–4.0 V, the capacity retention can achieve 80% after 50 cycles, which is three times as high as that of 1.5–4.0 V. The understanding and unveiling of voltage window dependent electrochemical reaction pathway can guide the practical application of LIB and further optimize the cycling stability.

2. Results and Discussion

The $\text{Na}_{0.76}\text{V}_6\text{O}_{15}$ nanorods obtained with the addition of 100 mg acetylene black are shown in Figure 1a,b. With the increasing of acetylene black from 0–100 mg, it is demonstrated that the crystallinity of $\text{Na}_{0.76}\text{V}_6\text{O}_{15}$ rises while that of V_2O_5 decreases (Figure 1c, Figure S2, Supporting Information). Meanwhile, it is found that the $\text{Na}_{0.76}\text{V}_6\text{O}_{15}$ samples with less acetylene black (0, 20, and 50 mg) exhibit an agglomerated state and irregularly shaped rods (Figure S1, Supporting Information). The amount of sodium dodecyl sulfate (SDS) is also regarded as an important factor in the synthesis of $\text{Na}_{0.76}\text{V}_6\text{O}_{15}$. The theoretical reaction ratio of SDS: V_2O_5 in $\text{Na}_{0.76}\text{V}_6\text{O}_{15}$ nanorods are 1:1, 1.3:1,

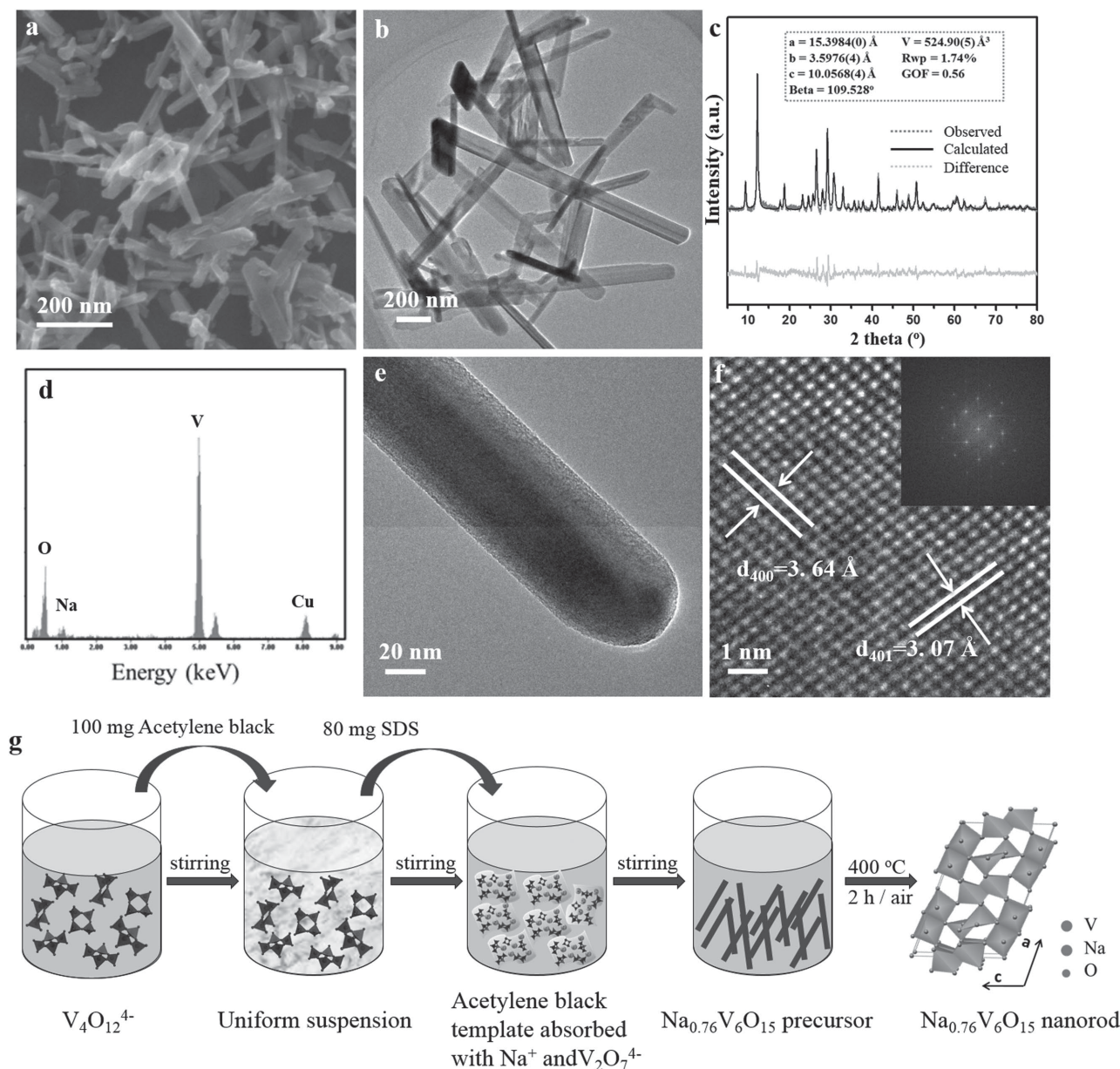


Figure 1. a) SEM image, b) TEM image, c) powder XRD pattern and XRD Rietveld refinement, d) EDS pattern, and e and f) HRTEM images of the $\text{Na}_{0.76}\text{V}_6\text{O}_{15}$ nanorod. The inset in (f) is the corresponding FFT pattern. g) Schematic of the formation of the $\text{Na}_{0.76}\text{V}_6\text{O}_{15}$ nanorods.

and 1.7:1 when the amount of SDS are 46, 60, and 80 mg, respectively. (Table S1, Supporting Information) Although the nanorods architecture can be obtained in all amount of SDS of 46, 60, and 80 mg (Figure S3, Supporting Information), the deficiency of SDS (46, 60 mg) leads to the formation of V_2O_5 . With the increasing amount of SDS from 46 to 80 mg, the XRD pattern peaks become sharp and intense, demonstrating the improvement of the crystallographic structure of $Na_{0.76}V_6O_{15}$ (Figure S4, Supporting Information). It can be supposed that the concentration of Na^+ should achieve a critical value which can result in the formation of $Na_{0.76}V_6O_{15}$ nanorods. During the stirring processes, the Na^+ provided by SDS is consumed continuously. When the concentration of Na^+ is lower than the critical value, the V_2O_5 forms. Thus, the excess Na^+ source (SDS) is needed to avoid the formation of V_2O_5 . Furthermore, the control experiments about annealing temperature are also conducted. As shown in Figure S5 in the Supporting Information, at a lower temperature of 350 °C (Figure S5a, Supporting Information), only nanoparticles are synthesized due to the limited driving force of nucleation and growth. The nanorod architecture can be obtained with the temperature of 400 °C (Figure 1a). However, when the temperature increased to 500 °C, nanorods tend to aggregate together (Figure S5b, Supporting Information). Thus, the $Na_{0.76}V_6O_{15}$ attained at 400 °C with addition amount of 100 mg acetylene black and 80 mg SDS is chosen to further investigate its crystal structure, morphology, and corresponding electrochemical performance. The XRD Rietveld refinement of $Na_{0.76}V_6O_{15}$ is performed by using total pattern solution (TOPAS) software. As shown in Figure 1c, all diffraction peaks are well indexed by a monoclinic $Na_{0.76}V_6O_{15}$ phase with small GOF value of 0.56. Figure 1b shows the TEM image of the $Na_{0.76}V_6O_{15}$ nanorods. The nanorods display uniform morphology with 50–100 nm wide and several micrometers long, which is consistent with the scanning electron microscopy (SEM) image results. The energy dispersive spectra (EDS) pattern of the $Na_{0.76}V_6O_{15}$ nanorods in Figure 1d shows that it only consists of O, Na, V, Cu elements. The Cu is attributed to the copper grid. High-resolution TEM (HRTEM) image shows clear lattice fringes with spacing of 3.07 and 3.64 Å, which are in agreement with that of the (401) and (400) planes of $Na_{0.76}V_6O_{15}$, respectively (Figure 1f). The fast Fourier transform (FFT) result in Figure 1f demonstrates the single crystalline nature of the as-obtained $Na_{0.76}V_6O_{15}$ nanorods.

Based on the experiment results above, the construct mechanism is proposed as follows (Figure 1g). The connection between V and O mainly depends on the pH value of the solution. The vanadium exists as a $V_4O_{12}^{4-}$ tetramer when the V_2O_5 sol is dispersed in the ethanol solution ($8 \cong PH \cong 6$).^[40,41] Then the $V_4O_{12}^{4-}$ tetramer absorbs on the acetylene black, which disperses evenly in the solution due to the effect of the surface tension. After SDS is added, the $V_4O_{12}^{4-}$ tetramer transforms into a VO_4^{3-} tetrahedron with the rise in pH value ($13 \cong PH \cong 9$) due to the ionization of the SDS.^[40,42] Then the acetylene black works as a template and adsorbs VO_4^{3-} and Na^+ . Attracted by the electrostatic interactions between the Na^+ species and the VO_4^{3-} species, the VO_4^{3-} tetrahedrons co-precipitate with Na^+ to form particles and then heterogeneous grow on the dispersed acetylene black. Finally, VO_4^{3-} tetrahedrons react with Na^+ in the acetylene black template which form $Na_{0.76}V_6O_{15}$

nanorods during the calcination process. The acetylene black plays three main roles in the whole process.^[43] (1) The dispersed acetylene black template works as a space blocking agent which effectively prevents the aggregation during the drying and calcination processes; (2) The acetylene black is consumed during the reaction, which provides the space for the oriented growth of the $Na_{0.76}V_6O_{15}$ crystal and results in the formation of $Na_{0.76}V_6O_{15}$ nanorods; (3) The combustion of the acetylene black provides extra heat for the formation of the $Na_{0.76}V_6O_{15}$ nanorods (Figure S6, Supporting Information).

Coin cells were assembled to investigate the electrochemical performance of the $Na_{0.76}V_6O_{15}$ nanorods. First, the $Na_{0.76}V_6O_{15}$ nanorods electrode was measured in a wide voltage window between 1.5 and 4.0 V versus Li^+/Li to obtain high capacity. Cyclic voltammetry (CV) curves measured at a scan rate of 0.1 mV s⁻¹ show three pairs of cathodic/anodic peaks, at about 3.24/3.34, 2.82/3.22, and 2.40/2.88 V (Figure 2a). However, an isolated oxidation peak at about 1.84 V is also captured. Traditionally, such irreversible electrochemical reaction leads to a poor cycling performance. Thus, the voltage window of CV curves is reduced to 2.0–4.0 V, which can avoid the formation of irreversible phase at 1.84 V (Figure 2b). Similar with that of 1.5–4.0 V, three pairs of oxidation and reduction peaks are observed. It is worth noting that the polarization of the redox peaks at 2.82/3.22 V under the voltage window of 1.5–4.0 V is three times as high as that of 2.0–4.0 V, which may be attributed to the irreversible electrochemical reaction at 1.84 V. The cycling performance within the two voltage windows is further evaluated by long-term galvanostatic charge/discharge testing (Figure 2c). Although, a high capacity of 213.5 mAh g⁻¹ is achieved under the voltage window of 1.5–4.0 V, only 55.5 mAh g⁻¹ is maintained after 50 cycles, corresponding to a capacity retention of 26%. To optimize the cycling performance of $Na_{0.76}V_6O_{15}$, the voltage window is reduced to 2.0–4.0 V. It is found that the capacity retention greatly increases to 80%, which is three times as high as that of 1.5–4.0 V, although the initial capacity of $Na_{0.76}V_6O_{15}$ is sacrificed.

In order to understand the improved cycling performance obtained within 2.0–4.0 V than that of 1.5–4.0 V, the ex situ SEM and TEM measurements of the $Na_{0.76}V_6O_{15}$ electrode after cycled are performed. Figures S7 and S8 in the Supporting Information are the SEM images of the $Na_{0.76}V_6O_{15}$ nanorods electrode discharged to 2.0 and 1.5 V, respectively. The morphology of $Na_{0.76}V_6O_{15}$ nanorods is maintained when discharge to 2.0 V, while broken after discharged to 1.5 V. The TEM and HRTEM images of the $Na_{0.76}V_6O_{15}$ nanorods after cycled within 1.5–4.0 V are shown in Figure S9a,b in the Supporting Information. The nanorods fracture into small pieces and aggregate together. Interestingly, HRTEM result suggests that the edge of nanorods is partially amorphous (Figure S9b, Supporting Information). TEM image shows that the nanorods after cycles within 2.0–4.0 V are preserved (Figure S9c, Supporting Information). Moreover, the lattice fringes in the HRTEM image are clearly visible, which indicates the excellent structural stability (Figure S9d, Supporting Information).

The in situ XRD technique has been applied to further investigate the insertion/extraction mechanism of the $Na_{0.76}V_6O_{15}$ nanorods with the two voltage windows. The 2θ are recorded from 21.0° to 35.5°, a range which can well reflect the structural

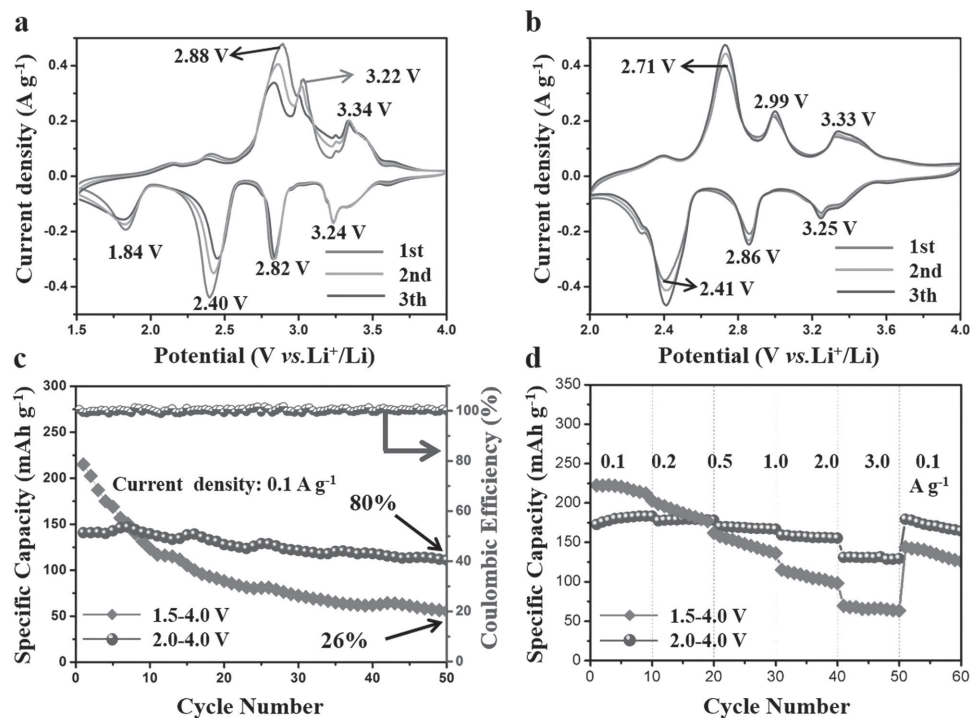


Figure 2. Cyclic voltammograms at a scan rate of 0.1 mV s^{-1} within a) $1.5\text{--}4.0 \text{ V}$ and b) $2.0\text{--}4.0 \text{ V}$. Cycling performance at a current density of c) 0.1 A g^{-1} and d) the rate performance of the $\text{Na}_{0.76}\text{V}_6\text{O}_{15}$ nanorods within $1.5\text{--}4.0 \text{ V}$ and $2.0\text{--}4.0 \text{ V}$.

changes of the $\text{Na}_{0.76}\text{V}_6\text{O}_{15}$ as electrode for LIBs during cycling within the two voltage windows at different current densities. It is demonstrated that a solid solution phase transformation occurs with the potential over 3.00 V , followed by twice two-phase transformations corresponding to the redox peaks of $2.86/2.99$ and $2.41/2.71 \text{ V}$ in the CV results, respectively (Figures 2b, 3a). Furthermore, the intensity of the diffraction peaks have not decreased after cycling at the current density of 100 , 200 , and 500 mA g^{-1} , respectively, which further indicates the high reversibility of the $\text{Na}_{0.76}\text{V}_6\text{O}_{15}$ nanorods under the voltage window of $2.0\text{--}4.0 \text{ V}$. Figure 3b shows the corresponding in situ XRD patterns collected within $1.5\text{--}4.0 \text{ V}$. An obvious asymmetric reaction pathway is observed during the lithiation and delithiation processes. Furthermore, the intensity of diffraction peaks decrease fast during cycling, which is consistent with the HRTEM image of the electrode after cycle. It is demonstrate the amorphism of crystal structure, which may results in the fast capacity degradation.

To further investigate the asymmetric reaction pathway in $\text{Na}_{0.76}\text{V}_6\text{O}_{15}$, the Rietveld structure refinement is applied with TOPAS. It can be confirmed that the phase of the electrode material is attributed to $\text{Na}_{0.76}\text{V}_6\text{O}_{15}$ without lithium ion insertion, when charged to 4.0 V (Figure 4b). There are three phase transformations while discharging to 2.5 V . (1) As the discharge process proceeds, the corresponding phase changes to $\text{Li}_{0.74}\text{Na}_{0.76}\text{V}_6\text{O}_{15}$ at 3.3 V (Figure 4c). (2) Another 0.5 Li^+ inserts into the lattice when discharged to 2.8 V and the phase transfers to $\text{Li}_{1.24}\text{Na}_{0.76}\text{V}_6\text{O}_{15}$ (Figure 4d). The electrode material undergoes a single phase reaction during the aforementioned processes. (3) The phase changes to $\text{Li}_{0.914}\text{Na}_{0.253}\text{V}_2\text{O}_5$ with expanding a -axis from 15.992 to 16.374 \AA , while discharged to

2.5 V (Figure 4e). Meanwhile, it can be found that the primary phase of $\text{Na}_{0.76}\text{V}_6\text{O}_{15}$ transforms to $\text{Li}_{0.914}\text{Na}_{0.253}\text{V}_2\text{O}_5$ at the beginning of the in situ test, which is regarded to be linked to a self-lithiation process during the fabrication process. The reactions and corresponding phase transitions above occur under the voltage window of both $1.5\text{--}4.0 \text{ V}$ and $2.0\text{--}4.0 \text{ V}$. However, less amount of $\text{Li}_{0.914}\text{Na}_{0.253}\text{V}_2\text{O}_5$ forms during delithiation under the voltage window of $1.5\text{--}4.0 \text{ V}$ than that of $2.0\text{--}4.0 \text{ V}$. To understand the above phenomenon, the deeper lithiation state is captured and refined, which is attributed to the framework of $[\text{Na}_{0.38}\text{V}_3\text{O}_7]$ (Figure 4f). By comparing with the original phase, $\text{Na}_{0.76}\text{V}_6\text{O}_{15}$, ionized oxygen, forms during the deep discharging process, which finally results in the formation of new phase. Two main differences are captured by comparing the in situ XRD results with different voltage windows. (1) The peak at 24.6° undergoes symmetrical transformations when charging and discharging in the voltage window of $2.0\text{--}4.0 \text{ V}$, but asymmetrical shift processes under the voltage window of $1.5\text{--}4.0 \text{ V}$. Although a two phase transformation occurs while discharging from 2.5 to 1.5 V , a solid solution transformation pathway is captured while charge under the voltage window of $1.5\text{--}4.0 \text{ V}$. These results are also consistent with the isolate peaks (1.84 V) in the CV curves. (2) Furthermore, the crystallinity degree decreases while further discharge to 1.5 V which may contribute to the excess lithium intercalation. It can be expected that the decrease of crystallinity degree leads to poor electron conductivity, increased polarization and overpotential.^[44,45] Meanwhile, the amorphization of crystal structure can lead to the diffusion of ionized oxygen.^[46] Thus, the framework of $[\text{Na}_{0.38}\text{V}_3\text{O}_7]$ cannot transform to that of $[\text{Na}_{0.253}\text{V}_2\text{O}_5]$ directly with the diffused ionized oxygen while discharge to

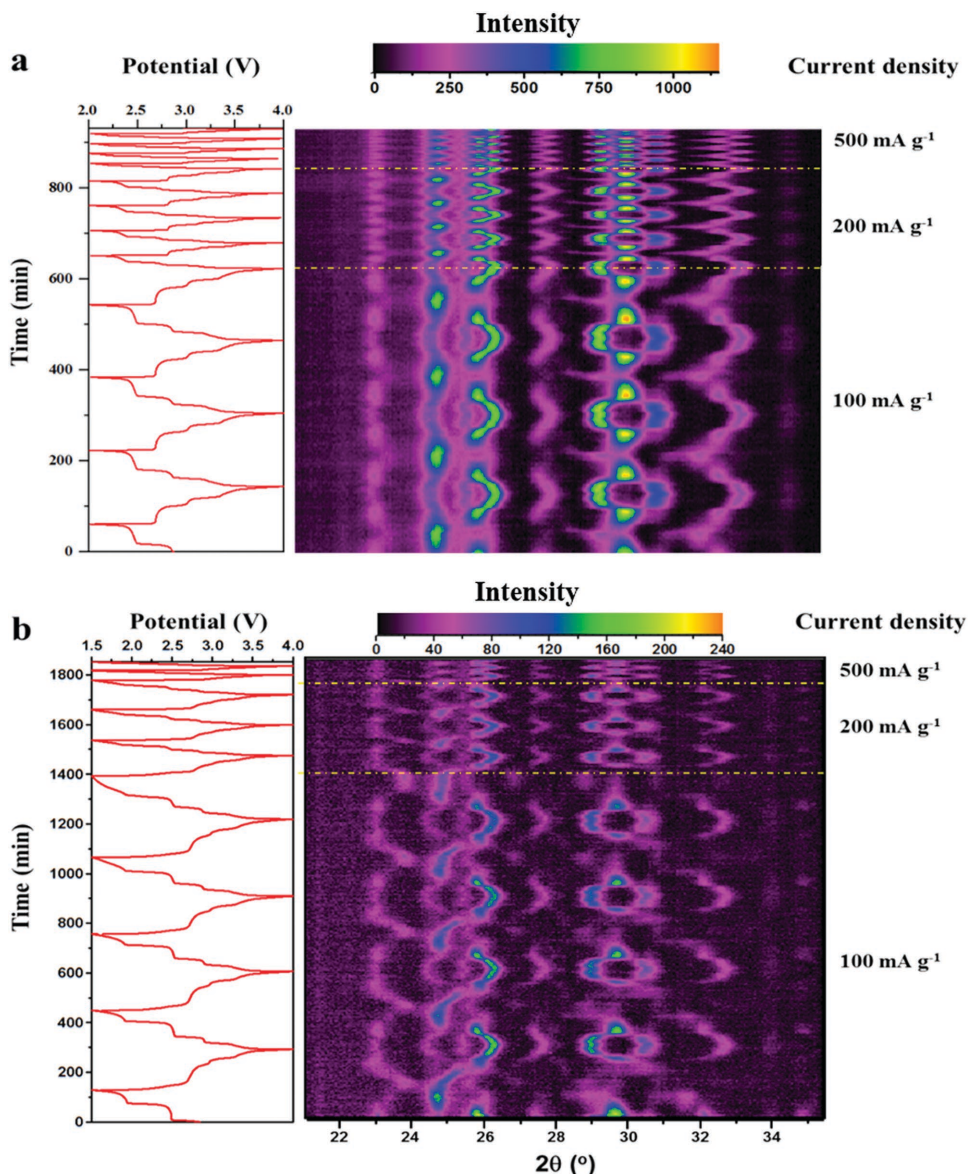


Figure 3. In situ XRD patterns collected during galvanostatic charge/discharge of $\text{Na}_{0.76}\text{V}_6\text{O}_{15}$ half-cell within a) 2.0–4.0 V and b) 1.5–4.0 V at different current densities.

1.5 V which undergoes a solid solution reaction. With lithium ion intercalation/deintercalation, the amorphization gets more and more severe, while the ionized oxygen aggregates, leading irreversible transferring between $[\text{Na}_{0.38}\text{V}_3\text{O}_7]$ and $[\text{Na}_{0.253}\text{V}_2\text{O}_5]$. Thus fast capacity fading is observed under voltage window of 1.5–4.0 V which can be avoided by reducing to 2.0–4.0 V.

The ex situ XPS, ex situ Raman spectroscopy and corresponding electrochemical analysis are further applied to verify the result deduced from in situ XRD. The XPS results of $\text{Na}_{0.76}\text{V}_6\text{O}_{15}$ with the states of original, charge to 4.0 from 2.0 V and charge to 4.0 from 1.5 V are displayed in Figure 5a–c, respectively. All of these three samples contain V^{4+} and V^{5+} , for which the binding energy of the $\text{V}2\text{p}_{3/2}$ band is 514.8 and 516.3 eV, respectively.^[47] Importantly, the peak area ratio of V^{5+} and V^{4+} changes greatly in different samples. In the original

sample and the cycled sample which charge to 4.0 from 2.0 V, the peak area ratio is 3.67 and 3.33, respectively. However, in the cycled sample which charge to 4.0 from 1.5 V, the peak area ratio of V^{5+} and V^{4+} greatly decreases to 1.53, which demonstrate the existence of irreversible reaction when cycling in the range of 1.5–4.0 V. The Raman spectrum of $\text{Na}_{0.76}\text{V}_6\text{O}_{15}$ powder and corresponding samples at different charge/discharge states are shown in Figure 5f. In original $\text{Na}_{0.76}\text{V}_6\text{O}_{15}$ powder, the highest frequency modes located at 142 cm^{-1} represents the stretching vibrations of particular V–O bonds in the (V1)O6, (V2)O6, and VO5 polyhedral.^[48] The Raman band at 259 cm^{-1} are assigned to the bending $\delta(\text{V–O–V})$. It is difficult to determine precisely the frequency distribution for these modes because of considerable coupling. The 440 cm^{-1} mode corresponds to the V2–O5 stretching and V1–O5–V3 bending vibrations.^[49]

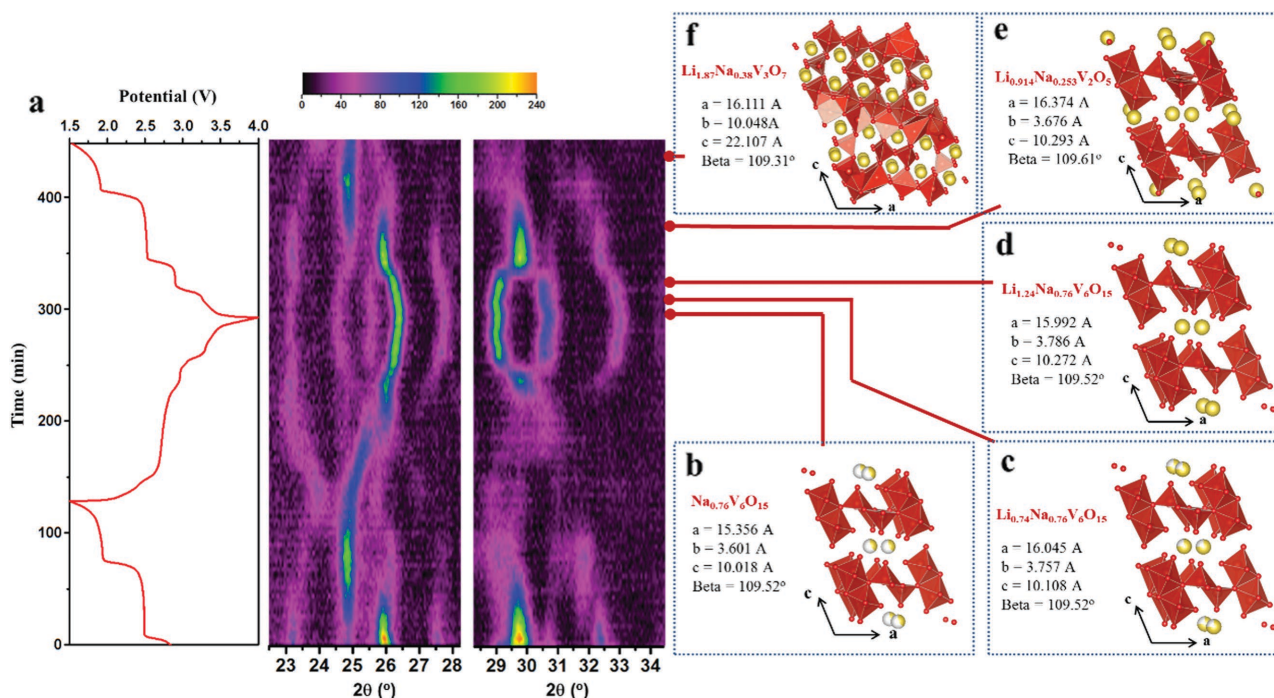


Figure 4. a) In situ XRD patterns collected during galvanostatic discharge/charge of $\text{Na}_{0.76}\text{V}_6\text{O}_{15}$ half-cell within 1.5–4.0 V. The crystal structure of the sample after XRD refinement during the discharging process of 4.0 to 1.5 V: b) 4.0 V, c) 3.3 V, d) 2.8 V, e) 2.5 V, f) 1.7 V.

(Figure S10, Supporting Information) The stretching vibrations of V3–O7 and the antisymmetric V1–O2–V1 stretching mode locate at 490 and 693 cm^{-1} , respectively. The mode at 1004 cm^{-1} originates from the V2–O6.^[48] However, almost all

the modes disappear when both discharge to 1.5 and 2.0 V, except the mode located at 142 cm^{-1} . The characteristic signatures located at around 1350 and 1600 cm^{-1} are attributed to the D-band (disordered carbon) and G band (graphitic carbon),

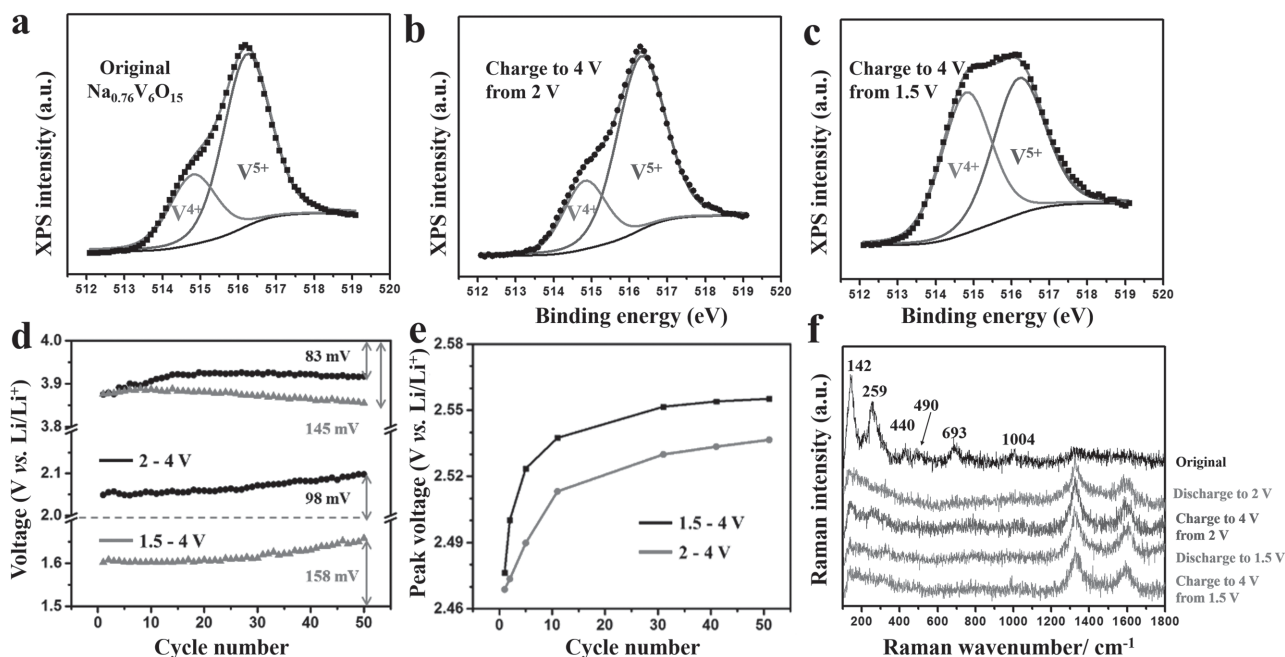


Figure 5. a) The X-ray photoelectron spectra of $\text{Na}_{0.76}\text{V}_6\text{O}_{15}$ with the states of original, b) charge to 4.0 from 2.0 V, and c) charge to 4.0 from 1.5 V. d) The voltage drop of $\text{Na}_{0.76}\text{V}_6\text{O}_{15}$ electrode. The batteries are charged to 4.0 V or discharged to 1.5 and 2.0 V firstly. Then, the batteries rest for 30 s. e) The changes of charge plateau voltages at ≈ 2.5 V when cycling within 1.5–4.0 and 2.0–4.0 V. f) Raman spectra of $\text{Na}_{0.76}\text{V}_6\text{O}_{15}$ with different electrochemical states.

respectively, due to the conductive carbon additives.^[50] When charge to 4.0 from 2.0 V again, the 259 cm⁻¹ mode is observed, while no obvious mode recovers in the Raman spectrum when charge to 4.0 from 1.5 V. Figure 5d illustrates the voltage drop at each cycle within the two voltage windows. When charged to 4.0 V under the voltage window of 2.0–4.0 V, the voltage drop decreases from 125 mV at the first 11 cycle and remains stable at ≈83 mV during the following cycles. However, the voltage drop start from 125 mV and increases to 145 mV after 50 cycles, when charge to 4.0 V under the voltage window of 1.5–4.0 V. High voltage drop is observed when discharged to 1.5 V (158 mV), which is 1.5 times to that of 2.0 V (98 mV). The changes of charge plateau voltage at ≈2.5 V are investigated (Figure 5e). The plateau voltage within the two voltage windows shift to higher potential as the cycling proceeds. The shifts of the plateau voltage make great differences with the two voltage windows. The plateau voltage shifts 68 mV (from 2.468 to 2.536 V) within 2.0–4.0 V, while that shifts 81 mV (from 2.475 to 2.556 V) within 1.5–4.0 V. These results above indicate that the polarization of the Na_{0.76}V₆O₁₅ electrode within 2.0–4.0 V is weaker than that within 1.5–4.0 V, which can benefit the cycling reversibility and control the diffusion of ionized oxygen. Eventually, the great enhanced stability is obtained by controlling the voltage window from 1.5–4.0 V to 2.0–4.0 V.

3. Conclusion

The Na_{0.76}V₆O₁₅ nanorods are applied to reveal the essence of voltage window dependent electrochemical reaction pathway. The corresponding structure evolutions are investigated through high time resolution in situ electrochemical XRD within different voltage windows of 1.5–4.0 and 2.0–4.0 V. The ionized oxygen is captured and demonstrated by combining in situ XRD and structure refinement when discharge to 2.0 V. Further decrease voltage to 1.5 V will lead to the asymmetric electrochemical reaction pathway, decrease of crystallinity degree due to the excess lithium intercalation. The amorphization of crystal structure can result in poor electron conductivity, the decrease of ionized oxygen migration energy, and increase of polarization and overpotential, which is further demonstrated by ex situ SEM, XPS, Raman spectroscopy, TEM, and corresponding electrochemical analyses. By optimizing the voltage window from 1.5–4.0 V to 2.0–4.0 V, the diffusion of ionized oxygen and amorphization of crystal structure are inhibited and the capacity retention greatly increases from 26% to 80%. Based on these results, the understanding of voltage window dependent electrochemical reaction pathway can guide the practical application of LIB and further optimize the cycling stability.

4. Experimental Section

Materials Synthesis and Characterization: V₂O₅, SDS, alcohol and acetylene black were analytical pure and purchased from Sinopharm Chemical Reagent Co., Ltd. (Shanghai, China). For a typical synthesis, the V₂O₅ sols were first prepared by a melt quenching process as reported previously.^[51] In brief, the V₂O₅ powder (30 g) was heated in air at 800 °C for 20 min, resulting in a molten liquid. Then, the melt was poured into deionized water under vigorous stirring to obtain the suspension, which

was then heated to the boiling point of water beforehand and cooled to room temperature naturally. After aging for 7 d, the brownish V₂O₅ dispersion was filtrated with a piece of filter paper (purchased from Whatman) to remove the aggregated V₂O₅ particles. Then, the filtrate (brownish V₂O₅ sols) was collected. For the synthesis of Na_{0.76}V₆O₁₅ nanorods, V₂O₅ sols (10 mL, 0.623 mmol) and acetylene black (100 mg) were added into alcohol (50 mL) and vigorously stirred for 30 min to obtain the homogeneous suspension. Then SDS (80 mg) was added into the suspension, which was further stirred for 2 h followed by drying at 70 °C to get precursor. In the end, the Na_{0.76}V₆O₁₅ nanorods were obtained by calcinating the precursor at 400 °C for 2 h. A series of experiments with different annealing temperatures and amounts of SDS and acetylene black were carried out in order to identify the optimal synthesis recipe. The XRD patterns of the samples were obtained with a D8 DISCOVER X-ray diffractometer, using Cu K α radiation ($\lambda = 1.5418 \text{ \AA}$). For in situ XRD testing, an electrochemical cell module with a beryllium window was used, while the slurry was directly cast on the beryllium window. Field emission scanning electron microscopy (FESEM) images and EDS were collected with a JEOL JSM-7100F microscope. TEM and HRTEM images were recorded with a JEM-2100F microscope. Raman spectra were acquired using a Renishaw RM-1000 laser Raman microscopy system. XPS measurements were performed using a VG MultiLab 2000 instrument.

Electrochemical Characterization: The electrochemical measurements were carried out using 2016 coin cells in a glove box filled with pure argon gas. The working electrodes were obtained using 70% Na_{0.76}V₆O₁₅ nanorods active material, 20% acetylene black, and 10% poly tetrafluoroethylene (PTFE). The mass loading of the electrode was 1.2–1.5 mg cm⁻². Lithium pellets were used as the anode. The electrolyte was composed of 1 M LiPF₆ dissolved in ethylene carbon (EC)/dimethyl carbonate (DMC) with a volume ratio of 1:1. Galvanostatic charge/discharge measurements were performed using a multichannel battery testing system (LAND CT2001A). CV was recorded using an electrochemical workstation (CHI 760D).

Supporting Information

Supporting Information is available from the Wiley Online Library or from the author.

Acknowledgements

M.Y.Y. and L.Z.Z. contributed equally to this work. This work was supported by the National Basic Research Program of China (2013CB934103), the National Key Research Program of China (2016YFA0202603), the National Natural Science Foundation of China (51302203, 51272197, 51521001), the National Natural Science Fund for Distinguished Young Scholars (51425204), the Hubei Province Natural Science Fund for Distinguished Young Scholars (2014CFA035), the Fundamental Research Funds for the Central Universities (WUT: 2015-PY-2, 2016III01, 2016III02, 2016III03, 2016III04, 2016III06), the China Scholarship Council (201606950049), and the International Postdoctoral Exchange Fellowship Program (20160025). Thanks to Prof. D. Y. Zhao of Fudan University, Prof. C. M. Lieber of Harvard University, and Prof. J. Liu of Pacific Northwest National Laboratory for strong support and stimulating discussions.

Received: April 28, 2016

Revised: May 27, 2016

Published online:

[1] M. Armand, J.-M. Tarascon, *Nature* **2008**, 451, 652.

[2] B. Kang, G. Ceder, *Nature* **2009**, 458, 190.

- [3] B. J. Landi, M. J. Ganter, C. D. Cress, R. A. DiLeo, R. P. Raffaele, *Energy Environ. Sci.* **2009**, *2*, 638.
- [4] H. Lee, M. Yanilmaz, O. Toprakci, K. Fu, X. Zhang, *Energy Environ. Sci.* **2014**, *7*, 3857.
- [5] D. Liu, G. Cao, *Energy Environ. Sci.* **2010**, *3*, 1218.
- [6] C. Zhu, P. Kopold, P. A. van Aken, J. Maier, Y. Yu, *Adv. Mater.* **2016**, *28*, 2409.
- [7] H. Liu, Y. Wang, L. Li, K. Wang, E. Hosono, H. Zhou, *J. Mater. Chem.* **2009**, *19*, 7885.
- [8] J. Cheng, G. Gu, Q. Guan, J. M. Razal, Z. Wang, X. Li, B. Wang, *J. Mater. Chem. A* **2016**, *4*, 2729.
- [9] A. M. Cao, J. S. Hu, H. P. Liang, L. J. Wan, *Angew. Chem. Int. Ed.* **2005**, *44*, 4391.
- [10] T. Zhai, H. Liu, H. Li, X. Fang, M. Liao, L. Li, H. Zhou, Y. Koide, Y. Bando, D. Golberg, *Adv. Mater.* **2010**, *22*, 2547.
- [11] P. Zhang, L. Zhao, Q. An, Q. Wei, L. Zhou, X. Wei, J. Sheng, L. Mai, *Small* **2016**, *12*, 1082.
- [12] S. Liang, Y. Hu, Z. Nie, H. Huang, T. Chen, A. Pan, G. Cao, *Nano Energy* **2015**, *13*, 58.
- [13] M. D. Wei, H. Sugihara, I. Honma, M. Ichihara, H. S. Zhou, *Adv. Mater.* **2005**, *17*, 2964.
- [14] H. Jiang, G. Jia, Y. Hu, Q. Cheng, Y. Fu, C. Li, *Ind. Eng. Chem. Res.* **2015**, *54*, 2960.
- [15] C. Niu, J. Meng, C. Han, K. Zhao, M. Yan, L. Mai, *Nano Lett.* **2014**, *14*, 2873.
- [16] W. Tang, Y. Zhu, Y. Hou, L. Liu, Y. Wu, K. P. Loh, H. Zhang, K. Zhu, *Energy Environ. Sci.* **2013**, *6*, 2093.
- [17] Y. L. Ding, Y. Wen, C. Wu, P. A. van Aken, J. Maier, Y. Yu, *Nano Lett.* **2015**, *15*, 1388.
- [18] M. S. Whittingham, *Chem. Rev.* **2004**, *104*, 4271.
- [19] Y. Xu, X. Han, L. Zheng, W. Yan, Y. Xie, *J. Mater. Chem.* **2011**, *21*, 14466.
- [20] C. Han, Y. Pi, Q. An, L. Mai, J. Xie, X. Xu, L. Xu, Y. Zhao, C. Niu, A. M. Khan, *Nano Lett.* **2012**, *12*, 4668.
- [21] S. Liang, T. Chen, A. Pan, D. Liu, Q. Zhu, G. Cao, *ACS Appl. Mater. Inter.* **2013**, *5*, 11913.
- [22] A. Pan, J.-G. Zhang, Z. Nie, G. Cao, B. W. Arey, G. Li, S.-q. Liang, J. Liu, *J. Mater. Chem.* **2010**, *20*, 9193.
- [23] Y.-Z. Zheng, H. Ding, E. Uchaker, X. Tao, J.-F. Chen, Q. Zhang, G. Cao, *J. Mater. Chem. A* **2015**, *3*, 1979.
- [24] G. Nagaraju, G. T. Chandrappa, *Mater. Res. Bull.* **2012**, *47*, 3216.
- [25] Y. Lu, J. Wu, J. Liu, M. Lei, S. Tang, P. Lu, L. Yang, H. Yang, Q. Yang, *ACS Appl. Mater. Inter.* **2015**, *7*, 17433.
- [26] C. Zhu, K. Song, P. A. van Aken, J. Maier, Y. Yu, *Nano Lett.* **2014**, *14*, 2175.
- [27] F. Zhang, M. S. Whittingham, *Electrochem. Commun.* **2000**, *2*, 69.
- [28] A. Selvaggi, F. Croce, B. Scrosati, *J. Power Sources* **1990**, *32*, 389.
- [29] H. Wang, W. Wang, Y. Ren, K. Huang, S. Liu, *J. Power Sources* **2012**, *199*, 263.
- [30] H. Liu, H. Zhou, L. Chen, Z. Tang, W. Yang, *J. Power Sources* **2011**, *196*, 814.
- [31] S. H. Ng, S. Y. Chew, J. Wang, D. Wexler, Y. Tournayre, K. Konstantinov, H. K. Liu, *J. Power Sources* **2007**, *174*, 1032.
- [32] L. Mai, L. Xu, C. Han, X. Xu, Y. Luo, S. Zhao, Y. Zhao, *Nano Lett.* **2010**, *10*, 4750.
- [33] C. Delmas, S. Brethes, M. Menetrier, *J. Power Sources* **1991**, *34*, 113.
- [34] H. X. Li, L. F. Jiao, H. T. Yuan, M. Zhang, J. Guo, L. Q. Wang, M. Zhao, Y. M. Wang, *Electrochem. Commun.* **2006**, *8*, 1693.
- [35] K. Shaju, G. S. Rao, B. Chowdari, *Electrochim. Acta* **2002**, *48*, 145.
- [36] K. M. Shaju, G. V. Subba Rao, B. V. R. Chowdari, *Electrochim. Acta* **2003**, *48*, 1505.
- [37] J. Shu, *J. Solid State Electrochem.* **2008**, *13*, 1535.
- [38] J. Shu, *Electrochem. Solid-State Lett.* **2008**, *11*, A238.
- [39] L. Mai, Q. Wei, Q. An, X. Tian, Y. Zhao, X. Xu, L. Xu, L. Chang, Q. Zhang, *Adv. Mater.* **2013**, *25*, 2969.
- [40] B. Vigolo, C. Zakri, F. Nallet, J. Livage, C. Coulon, *Langmuir* **2002**, *18*, 9121.
- [41] J. Livage, *Chem. Mater.* **1991**, *3*, 578.
- [42] O. Pelletier, P. Davidson, C. Bourgaux, C. Coulon, S. Regnault, J. Livage, *Langmuir* **2000**, *16*, 5295.
- [43] L. Zhang, K. Zhao, Y. Luo, Y. Dong, W. Xu, M. Yan, W. Ren, L. Zhou, L. Qu, L. Mai, *ACS Appl. Mater. Inter.* **2016**, *8*, 7139.
- [44] Q. Sun, Z.-W. Fu, *Electrochim. Acta* **2008**, *54*, 403.
- [45] A. Newport, C. J. Carmalt, I. P. Parkin, S. A. O'Neill, *Eur. J. Inorg. Chem.* **2004**, *2004*, 4286.
- [46] E. Boehm, J.-M. Bassat, P. Dordor, F. Mauvy, J.-C. Grenier, P. Stevens, *Solid State Ionics* **2005**, *176*, 2717.
- [47] V. L. Volkov, N. I. Kadyrova, G. S. Zakharova, M. V. Kuznetsov, N. V. Podval'naya, K. N. Mikhalev, Y. G. Zainulin, *Russ. J. Inorg. Chem.* **2007**, *52*, 329.
- [48] R. Baddour-Hadjean, A. Boudaoud, S. Bach, N. Emery, J. P. Pereira-Ramos, *Inorg. Chem.* **2014**, *53*, 1764.
- [49] R. Baddour-Hadjean, S. Bach, N. Emery, J. P. Pereira-Ramos, *J. Mater. Chem.* **2011**, *21*, 11296.
- [50] Q. L. Wei, Q. Y. An, D. D. Chen, L. Q. Mai, S. Y. Chen, Y. L. Zhao, K. M. Hercule, L. Xu, A. Minhas-Khan, Q. J. Zhang, *Nano Lett.* **2014**, *14*, 1042.
- [51] V. Petkov, P. N. Trikalitis, E. S. Bozin, S. J. Billinge, T. Vogt, M. G. Kanatzidis, *J. Am. Chem. Soc.* **2002**, *124*, 10157.